Journal of Atmospheric and Solar-Terrestrial Physics 72 (2010) 1221–1230

Contents lists available at ScienceDirect

Journal of Atmospheric and Solar-Terrestrial Physics

journal homepage: www.elsevier.com/locate/jastp

Determination of physical and radiant meteor properties using PFISR interferometry measurements of head echoes

Jonathan J. Sparks [a,b], Diego Janches [b,*], Michael J. Nicolls [c], Craig Heinselman [c]

[a] Department of Physics, University of Colorado, Boulder, CO, USA
[b] NWRA/CoRA Division, Boulder, CO, USA
[c] SRI International, Menlo Park, CA, USA

ARTICLE INFO

Article history:
Received 20 April 2010
Received in revised form
19 July 2010
Accepted 3 August 2010
Available online 11 August 2010

Keywords:
Radar
Meteor
Interferometry
HPLA
Head echo
Solar dust
SMC

ABSTRACT

Over the past decade, High Power and Large Aperture (HPLA) radars have been widely utilized for the study of sub-millimeter extraterrestrial particles via the detection of the meteor head-echo. These observations have been a successful tool in the study of the sporadic meteor background, however, they have been limited by the lack of precise knowledge of the particle's location within the radar beam and its absolute trajectory and velocity. This limitation prevents for example the accurate determination of the meteors radiant and orbit. Interferometry measurements of the head-echo has been proven to be a detection technique that satisfies this need. Unfortunately very few radars are capable of performing them. We have developed a methodology which takes advantage of the multi-receiving capabilities of the 450 MHz Poker Flat Incoherent Scatter Radar (PFISR) enabling us to utilize the phased array of crossed-dipoles as an interferometer. This new PFISR capability allows us to determine the instantaneous position of meteors within the radar beam. This enables us to determine absolute velocities and ultimately meteor radiant and orbit around the Sun. In this work, we present initial results from 9 h of observations during which 142 particles were individually detected by the three different receiving channels simultaneously. For these meteors absolute velocities were obtained and meteor dynamical, physical and radiant properties were derived.

1. Introduction

Over the past decade, High Power and Large Aperture (HPLA) radars have been widely utilized for astronomical and physical studies of sub-millimeter extraterrestrial particles and their effects in the upper atmosphere via the detection of the meteor head-echo (Janches et al., 2008, and reference therein). These observations have been a successful tool in the study of the Sporadic Meteor Complex (SMC), however, they have been limited due to the inability of most HPLA systems to determine precisely the particle's location within the radar beam and its absolute trajectory and velocity. These limitations introduce challenges when, for example, deriving meteoroid physical properties, requiring the use of large statistics and models (Dyrud and Janches, 2008; Janches et al., 2009). In addition, most of the HPLA systems only measure the meteor radial velocity (Janches et al., 2003; Sparks et al., 2009) which also prevents the accurate determination of the meteoroid traveling direction, its vector velocity, and consequently its orbital properties. This again entails the use of models to accurately understand the impact that the astronomical properties of the SMC has on the aeronomy of the Mesosphere and Lower Thermosphere (MLT) (Janches et al., 2006; Fentzke and Janches, 2008; Fentzke et al., 2009). Currently, there are 11 HPLA systems around the globe which are utilized, with different operational demand, for meteor head-echo observations. Table 1 in Janches et al. (2008) presents the main characteristics of 10 of these systems with the 11th being the Resolute Bay Incoherent Scatter Radar (RISR) in Arctic Canada, which has recently begun operations. Out of these systems, three of them have the capabilities to be used in interferometer mode, that is measure the phase difference of the returning radar pulse between separate receiving channels (see Section 2), allowing the determination of the precise location of the meteor head-echo in a pulse-to-pulse basis. These are the 46 MHz Middle and Upper (MU) Atmosphere radar in Japan (Sato et al., 2000; Nishimura et al., 2001), the 50 MHz Jicamarca Radio Observatory (JRO) in Peru (Chau and Woodman, 2004; Chau et al., 2007) and the ALTAIR system in the Marshals Islands (Hunt et al., 2004). All these systems are located at lower latitudes. At high-latitudes, the 930 MHz European Incoherent Scatter Radar (EISCAT) can perform tristatic measurements (Janches et al., 2002). That is it can observe a small common volume defined by overlapping the field-of-view of three antennas separated by few hundred kilometers. If a meteor event is detected within that volume and is strong

* Corresponding author.
E-mail address: diego@cora.nwra.com (D. Janches).

1364-6826/$ - see front matter © 2010 Elsevier Ltd. All rights reserved.
doi:10.1016/j.jastp.2010.08.004

enough to be detected by the three antennas, a vector velocity can be inferred. Unfortunately, EISCAT will soon cease to operate at this frequency thus preventing further studies at polar latitudes where the seasonal variation of the meteoric flux is largest (Janches et al., 2006; Fentzke et al., 2009; Sparks et al., 2009; Sparks and Janches, 2009).

The Poker Flat Incoherent Scatter Radar (PFISR; 65.126°N, 147.495°W) has been used for meteor head-echo studies since it begun operations in 2007 (Sparks et al., 2009). But until now it has been used strictly as a detection and ranging radar providing only the meteor radial velocity and range. As mentioned earlier, lacking information of the target azimuth and elevation it has made it impossible to track the trajectory of the detected meteors. In addition, meteor deceleration is also measured but with the inability to determine errors introduced by the range reduction of the meteor trajectory while it is being illuminated (Chau and Woodman, 2004). This results in the underestimation of derived dynamical meteoroid masses (Sparks et al., 2009). Upon the addition of interferometric capabilities not only can the aforementioned physical quantities be measured accurately but orbital properties can also be estimated allowing the study of the extra-terrestrial nature of the detected particles.

In this work we report a methodology by which PFISR can be operated as an interferometer. This proof-of-concept experiment is intended to demonstrate that meteor radiant and orbit determination is possible using PFISR. We focus only on the radiant results because it is more illuminating regarding the meteor sources. We performed this task by utilizing three groups of 256 crossed-dipole antennas (out of the 4096 total that make up PFISR) as separate receiving channels while we continue transmitting with the full array. Under this arrangement the phase-difference of the returning signal between channels can be measured and utilized to determine the azimuth and elevation of the radar target. This can be performed for each transmitted pulse. While radar interferometry is not a new concept these results represent the first successful attempt to add this capability to PFISR. In addition PFISR's operating wavelength is of one order of magnitude smaller than most meteor radars (generally operating between 20 and 50 MHz) as well as the HPLA radars that currently have interferometry capabilities. This wavelength difference allows computation of the radial velocity with far smaller error which will increase the fidelity of the computation of size, mass, and orbital parameters. In addition the small wavelength will prove significant in the analysis of 2π ambiguities and error estimates as well as the already well known frequency dependent detection differences.

Our paper is organized as follows: Section 2 describes the experimental setup and radar mode of operation; followed by our methodology of meteor characterization and interferometric calculation in Section 3. A discussion of measurement ambiguities are also presented in Section 4. Results and discussions are presented in Section 5 and conclusions and final remarks are presented in Section 6.

2. Experiment description

PFISR is a phased array radar consisting of 4096 crossed-dipoles. Meteor experiments with PFISR in the past were conducted by transmitting and receiving with the full array, that is all the dipoles connected to one receiving channel (Sparks et al., 2009). In order to operate PFISR in interferometer mode 3 groups of 256 dipoles were connected to separate receiving channels (referred as Dt0, Dt1, and Dt2 hereafter). These sub-arrays were located at the corner of the full array (Fig. 1). The receiver locations were placed such that they are sensitive to differences in the phase of the received signals from the same echo due to path length differences (Nishimura et al., 2001; Lau et al., 2006).

In order to perform these calculations we begin by defining a vector of the distance from the origin of our chosen coordinate system to the area centroid of receiver r. Note that "our chosen" coordinate system for this specific data set is the geodetic coordinate system presented in Fig. 1. All results presented in this work are with respect to this geodetic coordinate system. We define

$$\vec{d}_r = (d_x, d_y, d_z) \tag{1}$$

such that each component of the distance between receivers r and s is

$$x_{rs} = d_{xr} - d_{xs} \tag{2}$$

$$y_{rs} = d_{yr} - d_{ys} \tag{3}$$

$$z_{rs} = d_{zr} - d_{zs} \tag{4}$$

where r and s can range from 0 to 2 corresponding to receivers Dt0, Dt1, and Dt2. Therefore $\vec{x}_{rs}$ represents the distance in the x direction between each receiver pair (likewise for $\vec{y}_{rs}$ and $\vec{z}_{rs}$). In the case where a coordinate system has been chosen to reduce the system from a 3×3 to a 2×2 (see for example Lau et al., 2006) one of the above distance vectors will be a null vector (the basis vector that is not in the plane of the receivers). In our case all distance vectors shown above are nontrivial.

We defined the complex raw voltage recorded in channel r at a given Inter Pulse Period (IPP) as

$$z_r = I + iQ \tag{5}$$

From the raw voltage where the signature is present the phase difference between receivers is calculated by Nishimura et al. (2001)

$$\psi_{sr} = \tan^{-1}\left(\sum \frac{z_s}{z_r}|z_r|^2\right) \tag{6}$$

We also define the wave vector of the radiation returning from the target to the receivers as

$$\vec{k} = (k_x, k_y, k_z) \tag{7}$$

Once the phase difference between all receiver pairs (Dt0–Dt1; Dt1–Dt2; and Dt0–Dt2) have been estimated, $\vec{k}$ can be calculated through matrix inversion as (following the derivation presented in Nishimura et al., 2001, modified here for the case of a tilted array, i.e. all of the distance vectors in 2, 3, and 4 are nonzero)

$$\vec{k} = \begin{pmatrix} \sum x_{rs}^2 & \sum x_{rs}y_{rs} & \sum x_{rs}z_{rs} \\ \sum y_{rs}x_{rs} & \sum y_{rs}^2 & \sum y_{rs}z_{rs} \\ \sum z_{rs}x_{rs} & \sum z_{rs}y_{rs} & \sum z_{rs}^2 \end{pmatrix}^{-1} \begin{pmatrix} \sum \psi_{rs}x_{rs} \\ \sum \psi_{rs}y_{rs} \\ \sum \psi_{rs}z_{rs} \end{pmatrix} \tag{8}$$

The sums in Eq. (8) are carried out over all of the receiver pairs, this means that the indices r and s represent receiver pairs Dt0 & Dt1, Dt1 & Dt2, and Dt0 & Dt2, respectively. Each sum therefore has three terms each representing the aforementioned receiver pair. The traditional method of determining the echo's azimuth and elevation from the phase difference at three receivers involves the computation of the two components of the wave vector that the three receivers are sensitive to, or in other words Eq. (8) is diagonalized to two dimensions and solved. This method which is presented in most literature requires the use of a coordinate system that diagonalizes Eq. (8) (from three to two dimensions), namely a coordinate system where two of the three bases are in the plane of the three receivers. For most radars the three receivers coincide with a useful coordinate system. Since PFISR is mounted on a tilted platform it is an exception to this and we will therefore derive an interferometric algorithm

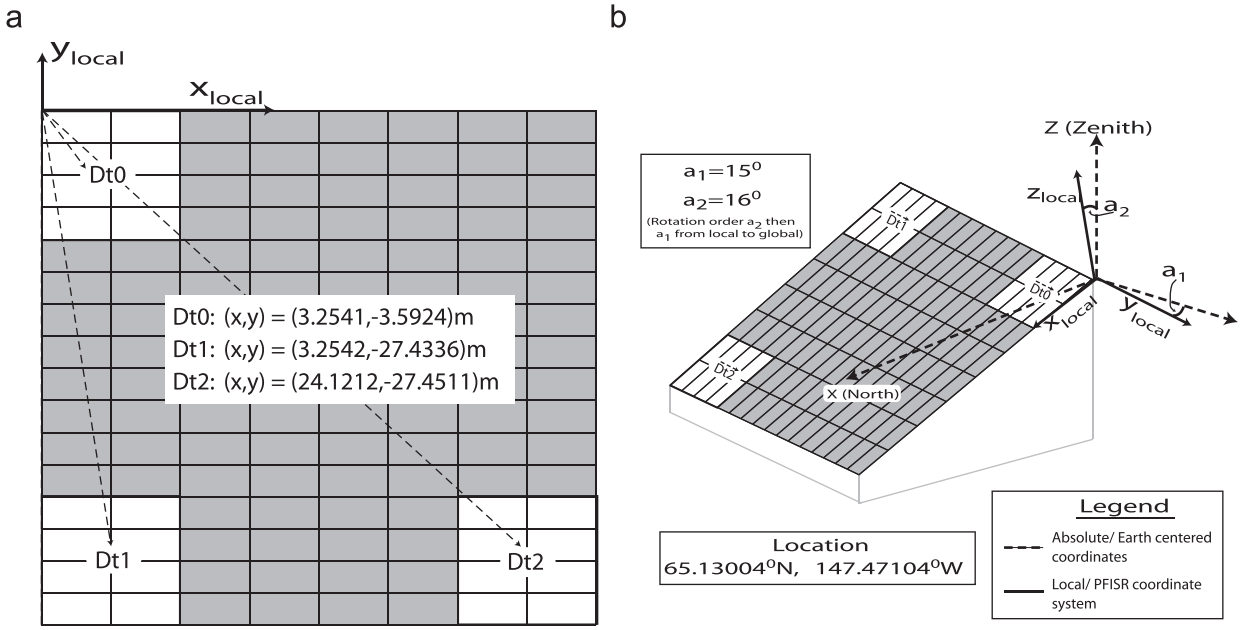

Fig. 1. (a) PFISR's panel layout. Each square represents a panel, each panel has 32 cross dipole antenna. The three receivers and their location with respect to PFISR's local coordinate system are shown in white at the three corners of the radar. The panels marked in grey are not used during the receiving process. (b) The relation of PFISR's local system to the geodic system as well as the rotation angles between the two systems and the absolute location of the radar.

that enables the computation of the echo's azimuth and elevation in any coordinate system. This method may seem inefficient because we are forced to invert a 3×3 matrix rather than a 2×2 matrix, however, it saves computational time since none of the results need to be transformed from one coordinate system to another and reduces the number of coordinate systems needed to solve this problem.

Since $\vec{k}$ points in the line-of-sight direction, then the azimuth and elevation of the meteor head echo for each single IPP can be calculated as

$$\phi = \tan^{-1}\left(\frac{k_x}{k_y}\right) \tag{9}$$

$$\alpha = \cos^{-1}\left(\frac{k_x^2+k_y^2}{|\vec{k}|}\right) \tag{10}$$

where ϕ and α are the meteors azimuth and elevation for the given IPP, respectively. The calculation from Eqs. (6) to (10) can be carried out for each IPP in which the meteor head echo is detected and thus determine all parameters that are tractable from a single IPP as a function of time in steps equal to the time interval between IPPs. For example the trajectory of the meteor across the beam (Fig. 2).

The results presented in the next section were derived from observations performed on July 9, 2009 from 07:22 to 15:53 UT. As in earlier experiments (Sparks et al., 2009) we utilized a sampling frequency of 1 μs (altitude resolution of 150 m) transmitting an uncoded pulse with a length of 90 μs every 2 ms. PFISR's operating frequency is 450 MHz and its peak transmitting power for this experiment was $\sim$1.3 MW. The half power half width for the full array is $\sim 1/2^{\circ}$.

3. Data analysis

The searching and analysis algorithms used for this experiment are similar to that described in Sparks et al. (2009). To pick out the detected meteor head echo events from hundreds of Gb of raw voltage data, we search for signals above a predefined threshold in the noise. The data above the noise are termed 'echoes' and are later classify as meteor head echoes (or not) following three main steps. The first is the 'Search and Echo Detection' step, in which an analysis of the background noise is first performed. After the background noise is estimated, the data are searched for samples that stand above the noise. The subset of data above the noise is identified as potential echoes if the signal is above the noise during several IPPs.

The second analysis step is the 'Echo Analysis' in which each potential echo is analyzed in greater detail through the calculation of all parameters that define the event. These parameters are listed below and some are shown in Fig. 2 (Sparks et al., 2009).

- Duration of the event defined as the difference in time between the first and last IPP in which the event was detected.
- Range for a given IPP. One value for each IPP in which the echo event is present.
- Radial Doppler velocity. One value for each IPP in which the echo event is present estimated from the doppler shift of the received signal (Janches et al., 2000b; Sparks et al., 2009).
- Signal-to-noise ratio (SNR). One value for each IPP in which the echo event is present.
- Three component position of the echo. One value for each IPP in which the echo event is present. The three components of the position are determined from the radar interferometry technique described in Section 2. The three components are given by the range, the azimuth and elevation. This three component vector is then converted into the cartesian system for computation of the velocity.
- Vector velocity. Although the radial velocity can be calculated for each IPP in which the echo is present, the vector velocity is estimated by least square fitting a line to the cartesian components of the echo position as a function of time. The fitting is performed after outliers have been thrown out. Outliers are defined as velocity points that have a standard deviation that is more than double of the mean about the best-fit line. It is important to note that outliers are not thrown from the data set but only excluded when making a linear fit.

- Acceleration. Derived from the least-square fit of a line to the doppler velocity as a function of time (after outliers have been thrown out). A correction due to range reduction effects is applied (see Section 5.1). This is now possible because the additional information given by interferometry.
- Average change in range for a single IPP. One value is calculated for the entire event by taking the average of the change in range for each consecutive set of IPP's (after outliers have been thrown out).
- Average change in doppler velocity for a single IPP. One value is calculated for the entire event by taking the average of the change in doppler velocity for each consecutive set of IPP's (after outliers have been thrown out).
- Average change in position for a single IPP. One value is calculated for the entire event by taking the average of the change in position for each consecutive set of IPP's (after outliers have been thrown out).

Because sometimes noise introduced in a single IPP may be large it will alter significantly the calculated parameters of the entire echo being analyzed. To reduce this effect all least square fitting is weighted by the SNR. In addition we ignore outliers only when making theoretical fits.

The third and final step is 'Echo Classification' during which each echo being defined by the parameters listed above is verified by visual inspection as a meteor event.

4. Ambiguity and accuracy for PFISR specific architecture

There is an ambiguity in the phase difference calculation introduced by the lack of knowledge of how many cycles the phase of the radar signal rotates between the moment of transmission and the moment of reception. Basically, once the signal is detected we do not know whether we are recording the first, tenth, or ten thousandth phase cycle. This manifests itself mathematically in the inverse trigonometric of Eqs. (6), (9) and (10) due to the impossibility of these functions to determine the number of phase cycles of the returned signal. In simple terms, these equations will always provide phases with values within $-\pi$ to π. Consequently, the difference in the path length between two waves recorded in separate receivers will always have values between $-\frac{1}{2}\lambda$ and $\frac{1}{2}\lambda$ (with λ is the transmitted wavelength). This implies that if the location of the meteor results in a path length difference between two receivers outside of this range, Eqs. (6), (9) and (10) will wrap the result to the 'principle volume of detection' (shown in Fig. 3) resulting in an incorrect location.

In order to understand the effect of this ambiguity in our measurements we defined as the ambiguity boundaries the limits in space that separate the unambiguous regions. That is, given two receivers, these boundaries are defined by the location in space where the path length difference is equal to an integer number of $\lambda/2$ given by

$$\sqrt{\sum(x_i+d_{ri})^2}-\sqrt{\sum(x_i-d_{si})^2}=\pm n\frac{\lambda}{2} \tag{11}$$

Where:

- Index i runs from 1 to 3 and represents the three cartesian spatial dimensions with: $x_1=x$, $x_2=y$, and $x_3=z$, respectively, as well as $d_{r1}=d_{rx}$, $d_{r2}=d_{ry}$, and $d_{r3}=d_{rz}$, respectively, for receiver r.
- Eq. (11) is a set of three equations representing the ambiguity surfaces formed by each set of receivers given by the indices r and s.
- n is an integer. The case of $n=1$ defines the principle boundaries, for the remain of the manuscript if n is unspecified it will be assumed to be equal to 1.

The effect of this ambiguity is displayed in Fig. 3 where a slice of the three functions given by Eq. (11) at 100 km for $n=1$ is shown together with PFISR's beam pattern. In this figure and Eq. (11) it can be seen that there is more than one place within the radar main beam that an echo can be located equally satisfying Eq. (11).

Fig. 4 shows an example of a meteor detected using PFISR in interferometer mode. Panels a and c show the phase difference while panels b and d show the trajectory of the meteor as calculated before and after unwrapping. The set of all trajectories in a small box about the main beam for any $n\pi$ ambiguity is shown in Fig. 5. The trajectory of the meteor was plotted not only in the central unambiguous zone but in all other possible locations. For all the calculations performed in this work we make the assumption that each meteor is closest to the center of the beam. Note that while the location is different for each n-value given by Eq. (11) the direction of the trajectory is the same for all of the possible paths. This is an important result because it allows for the determination of the meteoroid orbit even though the ambiguity is present since parallel paths so close (close being defined as with respect to the distance to the Sun) to each other will have essentially the same orbital parameters about the Sun. It should also be noted that there is an error introduced with an unknown phase offset between each of the receivers. Because this phase offset is constant in time it will result in a parallel translation of the trajectory; this translation will be less than a 1π ambiguity because anything larger would be wrapped. Because this offset generates a parallel translation less than the $n\pi$ ambiguity it does not introduce any additional considerations when computing radiants and orbits.

In addition to the error in location given by the ambiguity there is an error associated to each measurement based on how accurately the phase difference can be known. An error given by a rotation of the trajectory about its center rather than a translation would represent the error associated to a poor linear fit of the trajectory and would be caused only by phase resolution and not ambiguity (since ambiguity preserves relative distances or the direction of trajectory). Since the angular momentum vector about the Sun is perpendicular to the plane of orbit and the trajectory is within the plane of the orbit every degree of error included in the trajectory vector is at most directly translated to an error in the direction of the angular momentum vector of the meteor about the sun. Since the angular momentum of an orbit is the defining characteristic of an orbit any uncertainty in the angular momentum causes large uncertainty in the orbit. For this reason it is far greater to reduce error associated to the relative location of one measurement with respect to another than to reduce error of the absolute location with respect to any coordinate system. Or in other words the fidelity of the linear fit along the trajectory is far more important than knowledge of the trajectories absolute location. Since fidelity of the fit along the trajectory is not affected by the ambiguity but only phase resolution it is more important to focus on improving phase resolution than removing the error associated with the ambiguity.

Different system and receiver architectures will change the size of the ambiguity boundaries. If we consider a two-receiver system on a line the phase difference of a received signal from a source in the sky at an angle θ can be determined from simple geometry and is shown in

$$\Delta\phi=\left(\frac{2\pi}{\lambda}\right)d\sin(\theta) \tag{12}$$

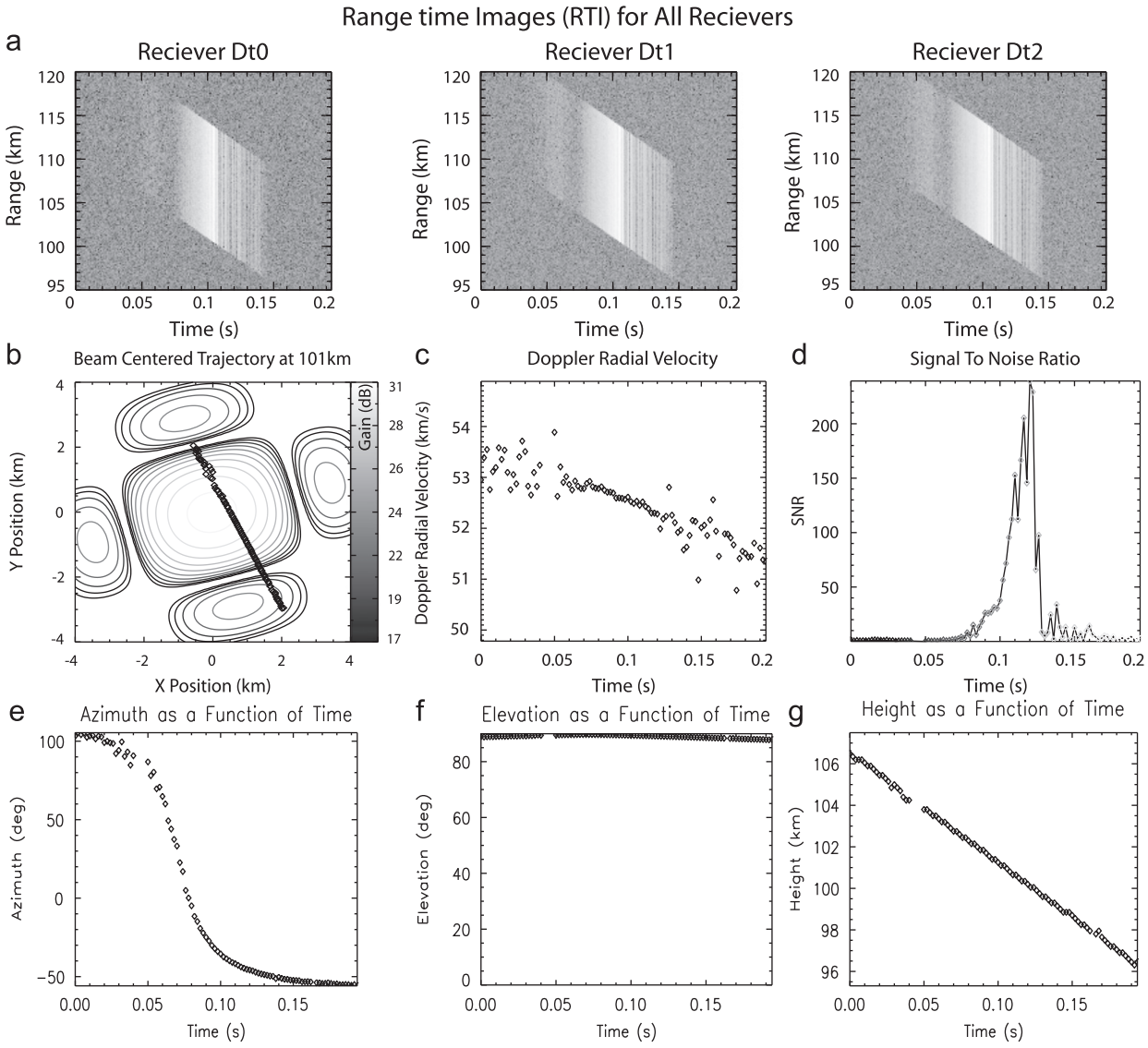

Fig. 2. Several of the important classifying parameters. All values are with respect to the geodetic coordinate system shown in Fig. 1. Each time step is one IPP. All plots are for the same meteor. (a) Range time images in power squared for all three channels, Dt0, Dt1, Dt2. (b) The trajectory of the meteor plotted against the beam pattern at the average altitude of detection. (c) The doppler radial velocity as a function of time. (d) The signal to noise ratio as a function of time. (e) Azimuth angle as a function of time. (f) Elevation angle as a function of time. (g) Height as a function of time.

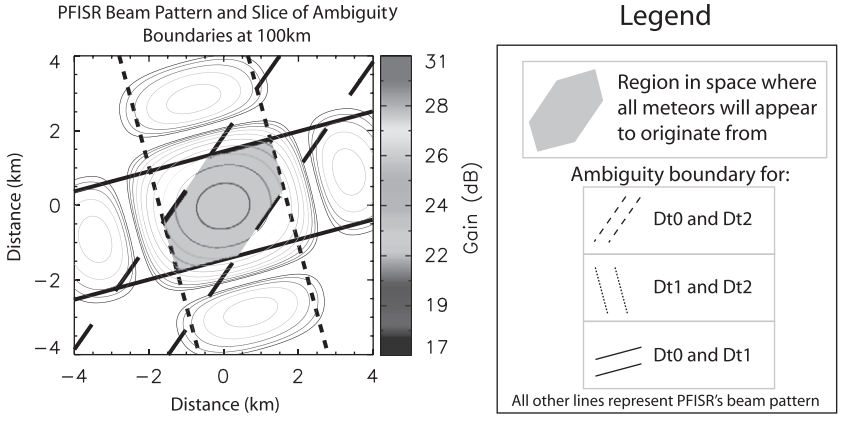

Fig. 3. Each parallel set of lines is actually a slice of the two sheeted surface given by Eq. (11) (for $n=1$) at 100 km altitude. The area between the lines is the area between the two sheets and is the region of space that is unambiguous. From this perspective the boundaries appear to form lines. This is because the zoom and aspect are set to represent the region about PFISR's main beam and not the ambiguity boundaries. Because their are three sets of receivers their are three sets of ambiguity surfaces shown by the six lines in this figure. The center of the intersection of all these surfaces is the region where all meteors will be assumed to be and has been termed the 'principle volume of detection'.

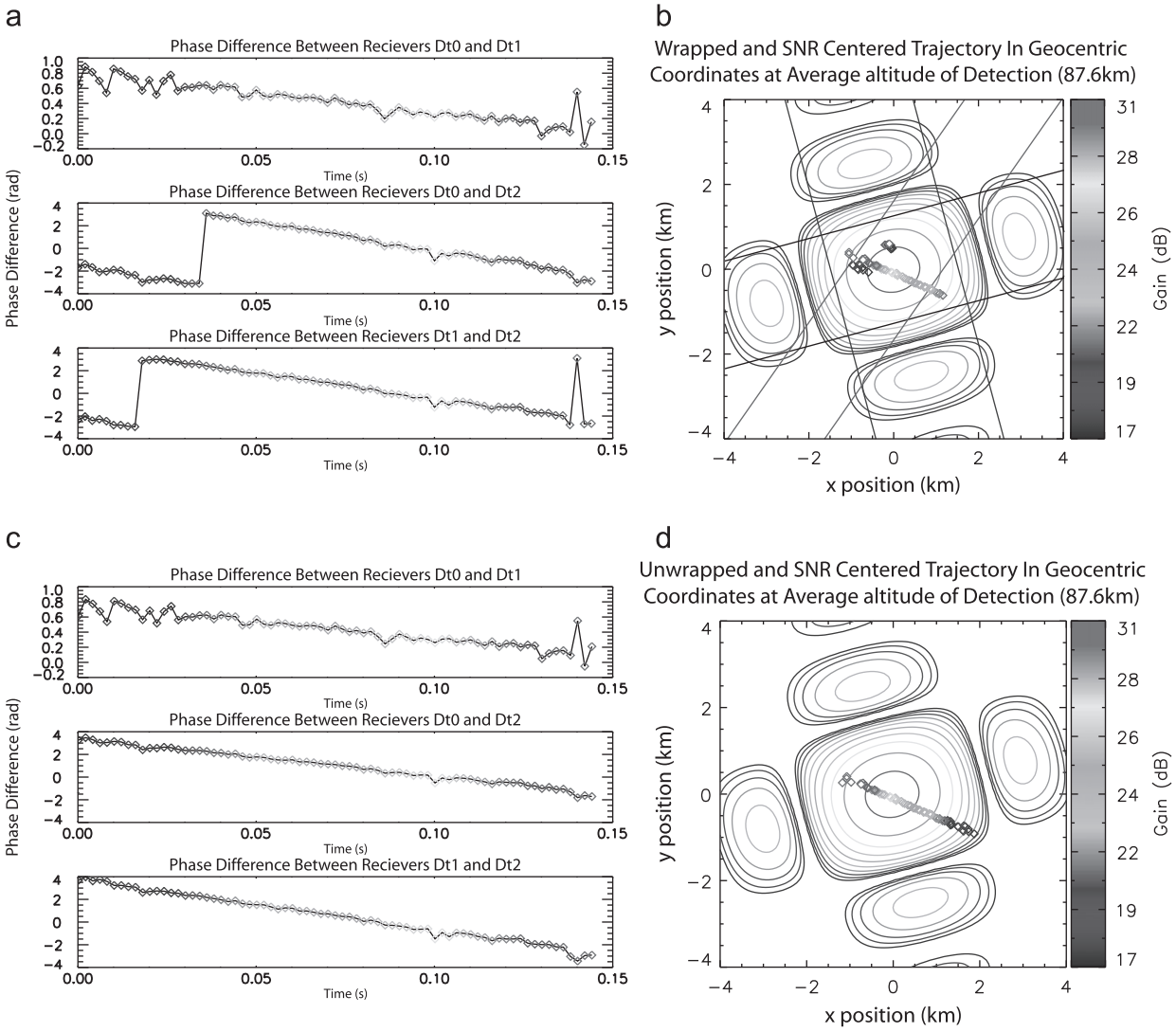

Fig. 4. Panels a and c show the phase difference as calculated before and after unwrapping. Panels b and d show the trajectory of the meteor as calculated before and after unwrapping.

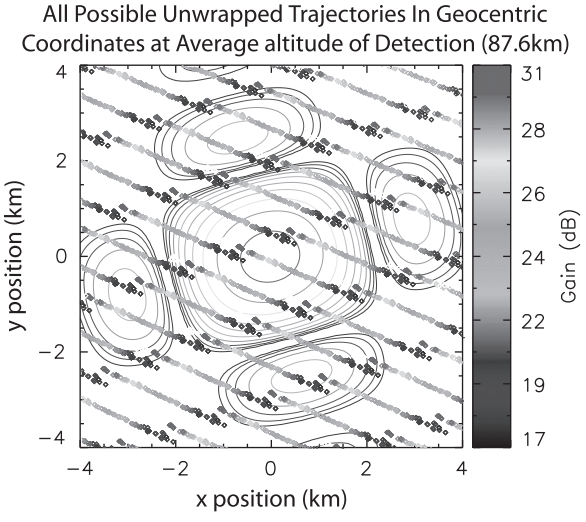

Fig. 5. Panels a and c show the phase difference as calculated before and after unwrapping. Panels b and d show the trajectory of the meteor as calculated before and after unwrapping.

In order to be unambiguous the phase difference must fall within $-\pi < \Delta\phi < \pi$ no matter what elevation angle the meteor is in the sky; in addition for all angles cosine ranges from $-1 < \cos < 1$, and the distance between the receivers must always be positive. Substituting these three constraints into Eq. (12) we see that if the distance between receivers satisfies $0 < d < \lambda/2$ the setup will be entirely unambiguous. Therefore the condition for unambiguous detection requires the receivers to be closer than one-half wavelength. Since PFISR has a 72 cm wavelength this is impossible. However, this demonstrates that decreasing the distance between the receivers increases in the distance between the ambiguity boundaries as represented in Fig. 3.

As discussed above error in phase is increased as the distance between receivers is decreased because moving receivers closer together requires a higher phase resolution to resolve the same position. This means that PFISR has the capability to make unambiguous measurements if the receivers can be moved close enough to cover the main beam and the first or first several sidelobes; this, however, would sacrifice phase resolution. By decreasing the phase resolution the three-dimensional bounding error bars about each measurement will increase. As discussed above the error associated with the direction of the meteors

trajectory is related to the bounding error bars of each individual measurement. It is also far more important to minimize errors associated in the direction of the trajectory than error associated with 2π ambiguities (when orbit determination is desired). In this respect the receiver arrangement used to gather the results presented here is likely the best option for determining the orbit of meteors about the Sun even though the meteors position is ambiguous up to several kilometers due to 2π ambiguities. The only apparent downside to this configuration is the possible decrease in counts due to the decreased sensitivity when not all antenna are utilized during receiving. In addition, because of the lack of precise knowledge of the location of the meteor within the gain pattern of PFISR, this configuration would require additional assumptions in order to use these measurements to understand the interaction between the electromagnetic radiation and the plasma formed during ablation (Dyrud and Janches, 2008; Janches et al., 2009). However, with Eqs. (11) and (12) an experiment to suit this or any other purpose (within PFISR's limitations) could be easily designed.

We make an estimation of the error in a given phase value by assuming the standard deviation of a phase estimate about the linear trend (see Fig. 4c) is approximately the error. From this method the average phase error is 11.5° from the mean. Fig. 6 shows the total error as calculated for all 142 detected meteors. To estimate the error in the radiant we start by making a host of assumptions and assuming that the error directly propagates through the computation without any attenuation or magnification. To do this we simply apply the phase error to error in the radiant. This gives us an error of about 11.5°.

Our next step is determining if the computation attenuates or magnifies the error. Error propagation theory tells us that error approximately grows or shrinks proportionally to the slope of the equation used (proper estimates use the sum in quadrature of the partial derivatives, however, this will suffice Taylor, 1996). Considering only one component of Eq. (8) after matrix inversion any given component will result in a combination of difference in receiver distances over its square times the phase. One order of difference in receiver distance will cancel and the error will decrease by about one over the receiver distance or 0.04 (about an order and a half). For computation of the azimuth and elevation the slope of the inverse tangent function is always less than or equal to 1 meaning that the error will either be smaller or equal after this computation. The inverse cosine has a slope always greater than or equal to one with a maximum about the wrapping point of $\pm\pi$, we estimate that this maximum should no more than double the error (an overestimation). At this point we have determined that for an average measurement there is less than a 1.15° error in the azimuth and elevation. From here a line is fit to the trajectory of the meteor and the azimuth and elevation of the trajectory is computed via the fit. This trajectory is then projected onto a map shown in Fig. 8. Here we will assume that because the error in a linear fit introduced by error in the data decreases as the number of points gets larger and an average meteor has more than 20 points of measurement, the error is no larger than the error in the data itself. Finally this suggests that an average point on the radiant map should have associated errors of the order of 1.15°.

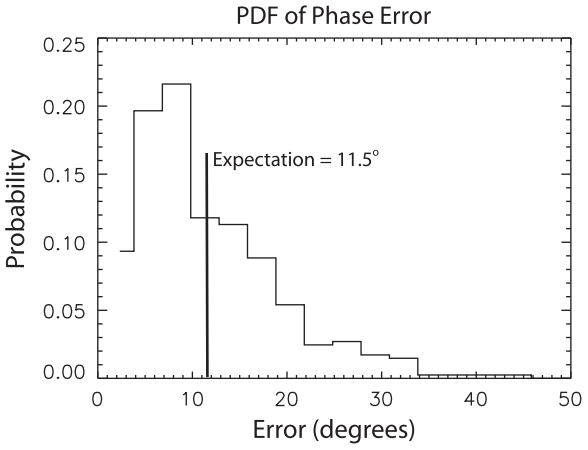

Fig. 6. The probability of a given phase error calculated by assuming that the standard deviation of the phase about the trend gives a good estimate of the error. This histogram was made by estimating the error once for each of the 142 meteors.

We have argued that the associated error in ecliptic longitude and latitude of the meteor radiant is, on average, less than one order of magnitude smaller than that of the phase. This computation has brought to light that the detected SNR is not the only thing that must be considered when estimating errors—the duration a meteor is observed also plays a role in the accuracy of radiant determination.

5. Results

5.1. Results of meteor observation

During the 9 h of observations a total of 142 meteors were observed in the three receivers. For all these events we were able to determine trajectories which in terms allowed for the computation of the acceleration, radius, dynamic mass, and radiant. As discussed in Section 3, because we have the meteor trajectory information, we can correct the range reduction effect to the acceleration computed from the doppler velocity as a function of time. This correction is given by Chau and Woodman (2004)

$$a = a_r + a_c \tag{13}$$

$$a_c = \frac{V\theta_r \cos(\phi)}{\Delta t} \tag{14}$$

where:

- a is the acceleration (corrected for range reduction).
- a_r the radial acceleration.
- a_c the acceleration correction factor due to range reduction effects.
- s the speed.
- θ_r the elevation angular coverage. The elevation angle swept out between the first and last time of detection (Chau and Woodman, 2004).
- ϕ the elevation angle of trajectory. Not the elevation of observation, the elevation of the trajectory (Chau and Woodman, 2004).
- Δt the duration of meteor detection.

In the past we have been able to measured only a_r (Janches et al., 2000b; Sparks et al., 2009). Because of the ability of correcting acceleration we can now compute the dynamical radius as (Bronshten, 1983)

$$Radius = \frac{3\rho_{air}V^2}{4\rho_{meteor}a} \tag{15}$$

where:

- ρ_{air} is the atmospheric density obtained from MSIS (Hedin, 1991).
- v the speed of meteor. For the uncorrected radius the radial velocity is used, otherwise the speed is used. This is due to the fact that speed cannot be calculated without interferometry.

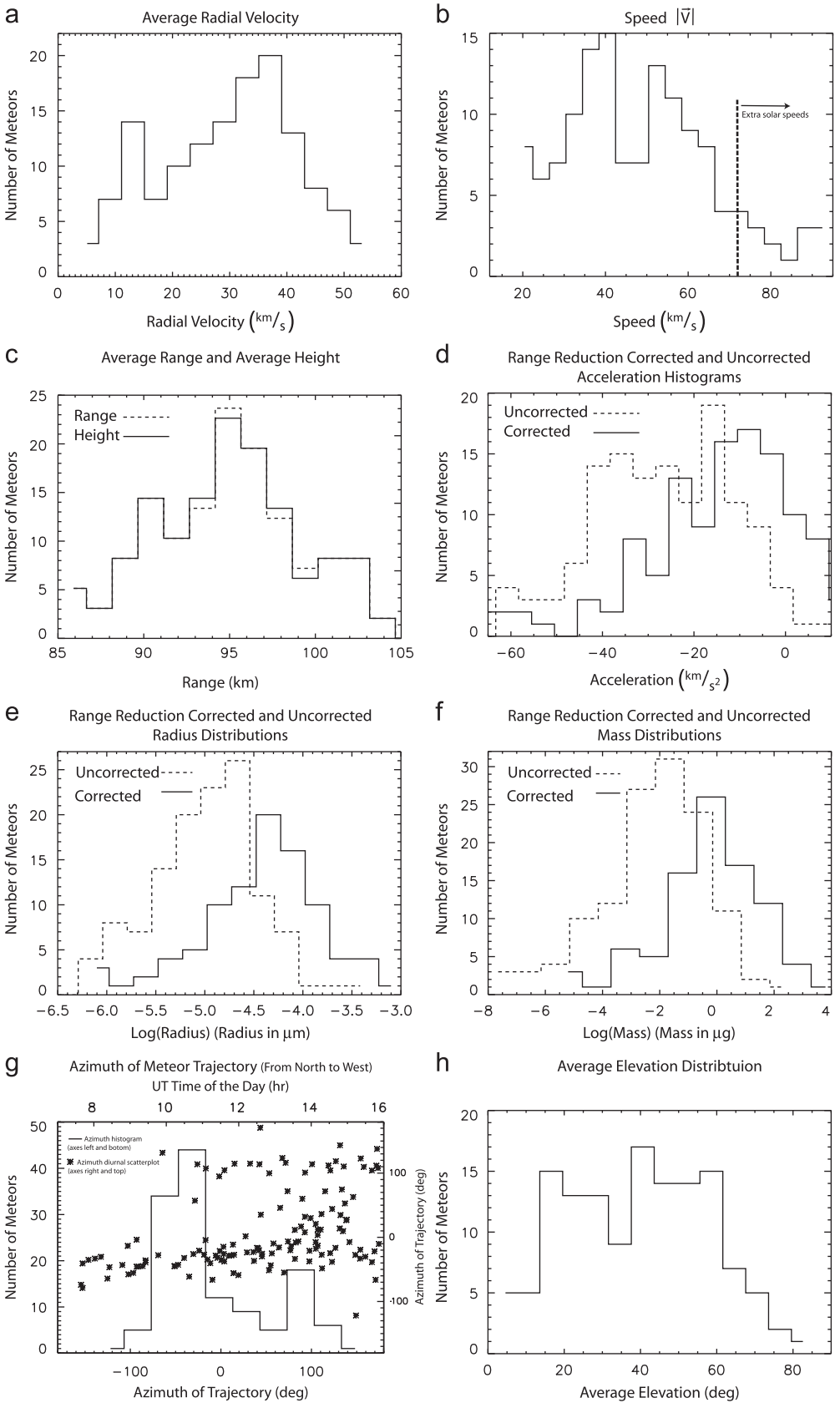

Fig. 7. Histograms of experimental results compared against the results if interferometry was not possible.

- ρ_{meteor} the density of meteor (assumed to be 3×10^3 kg/m^3).
- a the acceleration. For the uncorrected radius the radial acceleration is used.

Note that in previous work, we have utilized the radial velocity and uncorrected acceleration (Janches et al., 2000b; Sparks et al., 2009). The dynamic mass is then computed by multiplying the volume of the meteor by the assumed meteoroid density considering the particle to be spherical in shape. The difference between the corrected and uncorrected dynamic mass is therefore due only to the use of the corrected and uncorrected acceleration and the absolute velocity instead of the radial one used in past works. As in all quantities the uncorrected values are what have traditionally been obtained without the capability of interferometry where the corrected values have been adjusted given the knowledge of the meteors absolute position.

Histograms of the derived quantities are shown in Fig. 7. An interesting result is observed in panel b of this figure where the distribution of the meteoroid absolute velocity is shown. Although 142 meteors does not provide significant statistics, it is evident from this figure the existence of two velocity populations. One with a peak at 35–40 km/s and a faster one with a peak velocity of the order of 50–55 km/s. The velocity of the slower population is consistent with the detection of particles from the Helion and North Toroidal sources, considering the portion of the sky that was visible during our observing period (see Fig. 8). The faster population has speeds consistent with meteoroids originating from the North-Apex source (Jones and Brown, 1993; Taylor, 1995; Taylor and Elford, 1998; Fentzke and Janches, 2008). Interestingly, the magnitude of both peaks is similar and a bias towards fastest meteors does not appear to be present, at least in these observations. These distributions seem to agree well with those predicted by dynamical models of the SMC (Wiegert et al., 2009). Additional planned observations will provide the necessary statistics to look into this issue in more detail although at these latitudes we expect the measured velocity distributions to vary significantly with season (Janches et al., 2006; Fentzke et al., 2009). This is simply because during certain periods some of the sources are below the local horizon (Janches et al., 2006; Fentzke et al., 2009; Sparks and Janches, 2009).

Panel b also shows that 11% (16 events in total) of the detected meteors are above the escape speed of the solar system (72 km/s). Five events above 72 km/s are low SNR events while the rest are above average SNR events, in addition one event is a very high SNR event. This suggests that these velocities are obtained independently of experimental uncertainties (i.e. strong SNR generally provides robust estimate of velocities and phases) indicating that at least a portion of these events are real hyperbolic meteoroids. This, however, will need to be studied in more detail before the percentage of extra solar meteors and their properties can be estimated.

Additionally, it can be observed from Fig. 7d that the differences between corrected and uncorrected decelerations are of the order of 15–20 km/s^2. This is in agreement with our previous estimates reported in Sparks et al. (2009). An important result is that the use of radial velocity and uncorrected acceleration results in an underestimation of the dynamical mass of 1–2 orders of magnitude. The resultant corrected dynamical mass distribution peaks at $\sim$1 μg in agreement with results derived from our model of the Meteor Input Function (MIF) reported by Fentzke and Janches (2008) and Fentzke et al. (2009).

Finally, Fig. 8 shows the radiant of the 142 detections plotted in the ecliptic plane. This figure is in the Sun-centered coordinate frame of reference (the relative motion of the earth is removed) where 0° indicates local noon and the position of antihelion at 180° indicates local midnight. The location of the six sporadic meteoroid sources is also displayed in this figure along with the relative zenith trajectory of PFISR's beam center path (red solid line) during the observed period. Most of the meteors observed do not appear to originate from the SMC apparent source regions. The fact that so few of the detected meteors lie within the 1-sigma regions of the various radiants is, we believe, due primarily to reduced sensitivity of this experiment to meteors from those directions. While a full analysis of this sensitivity has not been completed, we expect that longer duration runs in different seasons will provide the necessary larger statistics to better complete the picture of those radiants (Jones and Brown, 1993;

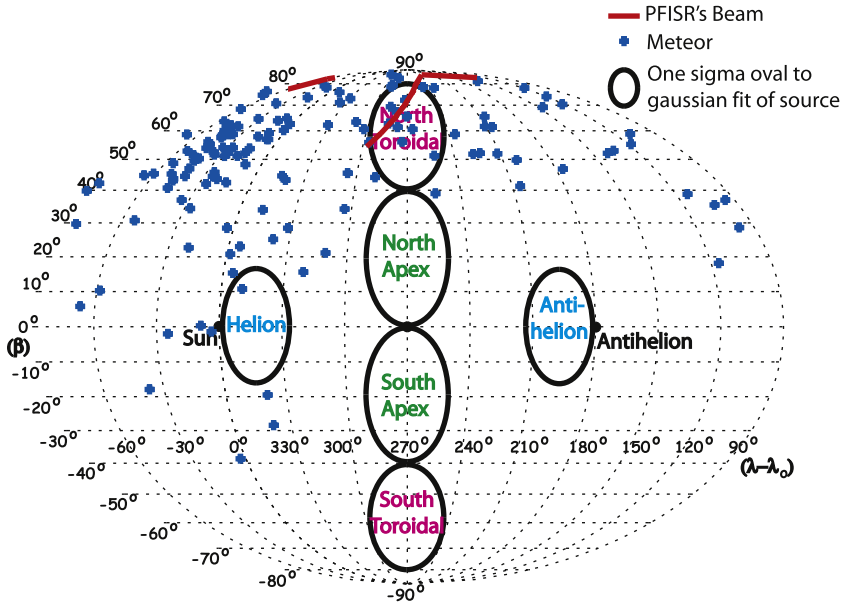

Fig. 8. All 142 meteors shown on a radiant map along with PFISR's beam during the observation time. The accepted six sporadic meteor sources derived from previous investigations are represented by a theoretical one-sigma ellipses (Fentzke et al., 2009 and reference therein).

Chau and Woodman, 2004; Campbell-Brown, 2008; Galligan and Baggaley, 2005). As expected, most of the detections have high ecliptic latitudes, since PFISR is located at arctic latitudes. There are few events, however, which ecliptic latitudes are below the ecliptic equator. These are most likely erroneous since PFISR should not be able to observe that part of the sky and are probably due to very weak SNR meteors which introduce large errors when computing the phases.

6. Conclusion

In this paper we have reported the first successful radar observations of meteor head echoes using PFISR in interferometer mode. The added capability to this facility offers a great tool to investigate the radio science of meteors, their astronomical nature and its impact into the aeronomy of the upper atmosphere. PFISR's new capabilities are enticing in particular because of its high latitude location. At these high latitudes, where the meteor flux is highly variable, there are a number of phenomena related to ice particles in the mesosphere for which it is believed this flux provides the necessary condensation nuclei (i.e. noctilucent clouds, polar mesospheric summer echoes, etc.). We have shown that using PFISR in this mode with the current receiver arrangement introduces significant uncertainties associated with 2π ambiguities that can lead to errors on the echo position of the order of several kilometers in translation with respect to the chosen coordinate system. This is in particular a problem when studying the plasma and ablation processes that form the head-echo for which precise knowledge of the location of the meteor within the radar beam is needed (Dyrud and Janches, 2008; Janches et al., 2009). Some of these errors can be minimized or eliminated if the sub-array forming the receivers are selected to be closer together. However, that adds inaccuracies to the phase measurements which are benefited if the receivers are further apart. We are currently designing experiments to find the best compromise between these two issues.

We have estimated dynamical, physical and orbital parameters for the 142 meteors detected in all three receivers during the 9 h observation reported here. We also have shown that errors introduced in the radial velocity due to range reduction effect can underestimate dynamical mass by 1–2 orders of magnitudes. The resulted corrected dynamical mass distribution peaks at $\sim 1\,\mu g$ in agreement with results derived from our MIF model (Fentzke et al., 2009). Finally, radiants information for all the meteors detected by the three receivers were presented.

Acknowledgements

PFISR is operated by SRI International under NSF ATM-0608577 cooperative agreement. D.J. and J.J.S. were supported under NSF Grants AST-0908118 and AGS-0525655 and AGS-0634650 to NorthWest Research Associates, Inc. The authors wish to thank T. Nakamura and K. Nishimura for their help with the interferometry calculations and J.T. Fentzke for help on Fig. 7.

References

Bronshten, V., 1983. Physics of Meteoric Phenomena. D. Reidel Publishing Co.
Campbell-Brown, M.D., 2008. High resolution radiant distribution and orbits of sporadic radar meteoroids. Icarus 196, 144–163.
Chau, J.L., Woodman, R., 2004. Observations of meteor head-echoes using the jicamarca 50 MHz radar in interferometer mode. Atmos. Chem. Phys. 3 (6), 6063–6091.
Chau, J.L., Woodman, R.F., Galindo, F., 2007. Sporadic meteor sources as observed by the Jicamarca high-power large-aperture VHF radar. Icarus 188, 162–174.
Dyrud, L.P., Janches, D., 2008. Modeling the meteor head-echo using Arecibo observations. J. Atmos. Solar Terr. Phys. 70, 1621.
Fentzke, J.T., Janches, D., 2008. A semi-empirical model of the contribution from sporadic meteoroid sources on the meteor input function observed at arecibo. J. Geophys. Res. (Space Phys.) 113 (A03304).
Fentzke, J.T., Janches, D., Sparks, J.J., 2009. Latitudinal and seasonal variability of the micrometeor input function: a study using model predictions, Arecibo, and PFISR observations. J. Atmos. Solar Terr. Phys. 71, 653.
Galligan, D.P., Baggaley, W.J., May 2005. The radiant distribution of AMOR radar meteors. Mon. Not. R. Astron. Soc. 359, 551–560.
Hedin, A.E., 1991. Extension of the MSIS thermosphere model into the middle and lower atmosphere. J. Geophys. Res. 96, 1159–1172.
Hunt, S., Oppenheim, M., Close, S., Brown, P., McKeen, F., Minardi, M., 2004. Determination of the meteoroid velocity distribution at the earth using high-gain radar. Icarus 168.
Janches, D., Close, S., Fentzke, J.T., 2008. A comparison of detection sensitivity between ALTAIR and Arecibo meteor observations: Can high power and large aperture radars detect low velocity meteor head-echoes. Icarus 193, 105–111.
Janches, D., Dyrud, L.P., Broadley, S.L., Plane, J.M.C., 2009. First observation of micrometeoroid differential ablation in the atmosphere. Geophys. Res. Lett. 36, 6101.
Janches, D., Heinselman, C., Chau, J., Chandran, A., Woodman, R., 2006. Modeling the global micrometeor input function in the upper atmosphere observed by high power and large aperture radars. J. Geophys. Res. 111.
Janches, D., Mathews, J., Meisel, D., Zhou, Q., 2000b. Micrometeor observations using the arecibo 430 mhz radar: I. determination of the ballistic parameter from measured doppler velocity and deceleration results. Icarus 145, 53–63.
Janches, D., Nolan, M., Meisel, D., Mathews, J., Zhou, Q., Moser, D., 2003. On the geocentric micrometeor velocity distribution. J. Geophys. Res. 108 (A6), 1222 doi:10.1029/2002JA009789..
Janches, D., Pellinen-Wannberg, A., Wannberg, G., Westman, A., Haggsstrom, I., Meisel, D., 2002. Tristatic observations of meteors using the 930 mhz eiscat radar system. J. Geophys. Res. 107 (A11), 1389 doi:10.1029/2001JA009205..
Jones, J., Brown, P., 1993. Sporadic meteor radiant distribution: orbital survey results. Mon. Not. R. Astron. Soc. 265, 524–532.
Lau, E.M., Avery, S.K., Avery, J.P., Janches, D., Palo, S.E., Schafer, R., Makarov, N.A., Jul. 2006. Statistical characterization of the meteor trail distribution at the South Pole as seen by a VHF interferometric meteor radar. Radio Sci. 41, 4007.
Nishimura, K., Sato, T., Nakamura, T., Ueda, M., 2001. High sensitivity radar-optical observations of faint meteors. IEICE Trans. Commun. E84-C (12).
Sato, T., Nakamura, T., Nishimura, K., 2000. Orbit determination of meteors using the mu radar. IEICE Trans. Commun. E83-B (9).
Sparks, J.J., Janches, D., 2009. Latitudinal dependence of the variability of the micrometeor altitude distribution. Geophys. Res. Lett. 36, L12105, doi:10.1029/2009GL038485.
Sparks, J.J., Janches, D., Nicolls, M.J., Heinselman, C.J., 2009. Seasonal and diurnal variability of the meteor flux at high latitudes observed using PFISR. J. Atmos. Solar Terr. Phys. 71, 644–652, doi:10.1016/j.jastp.2008.08.009.
Taylor, A., 1995. The harvard radio meteor project meteor velocity distribution reappraised. Icarus 116, 205–209.
Taylor, A., Elford, W., June 1998. Meteoroid orbital element distribution at 1 au deduced from the harvard radio meteor project observations. Earth Planets Space 50, 569–575.
Taylor, J.R., 1996. An Introduction to Error Analysis: The Study of Uncertainties in Physical Measurements, second ed. University Science Books.
Wiegert, P., Vaubaillon, J., Campbell-Brown, M., May 2009. A dynamical model of the sporadic meteoroid complex. Icarus 201, 295–310.